Chemical inhibition of stomatal differentiation by perturbation of the master-regulatory bHLH heterodimer via an ACT-Like domain

Ayami Nakagawa[1]*, Krishna Mohan Sepuru[2,3]*, Shu Jan Alicia Yip[1]*, Hyemin Seo[2,3], Calvin M. Coffin[2,3], Yasutomo Segawa[4], Rie Iwasaki[1], Hiroe Kato[1], Stephanie Kim[3], Yusuke Aihara[1,5], Toshinori Kinoshita[1], Kenichiro Itami[1], Soon-Ki Han[1,6], Kei Murakami[1,5,7+], and Keiko U. Torii[1,2,3+]

[1]Institute of Transformative Bio-Molecules, Nagoya University, Nagoya, Aichi, 464-8601, Japan

[2]Howard Hughes Medical Institute, The University of Texas at Austin, Austin, TX 78712 USA

[3]Department of Molecular Biosciences, The University of Texas at Austin, Austin, TX 78712 USA

[4]Institute for Molecular Science and SOKENDAI, Myodaiji, Okazaki, 444-8585, Japan

[5]PRESTO, Japan Science and Technology Agency (JST), Chiyoda, Tokyo 102-0076, Japan

[6]Institute for Advanced Research (IAR), Nagoya University, Nagoya, Aichi, 464-8601, Japan

[7]Department of Chemistry, Kwansei Gakuin University, Sanda, Hyogo 669-1330, Japan

*These authors contributed equally

+Corresponding authors

kei.murakami@kwansei.ac.jp

ktorii@utexas.edu

Selective perturbation of protein interactions with chemical compounds enables dissection and control of developmental processes. Differentiation of stomata, cellular valves vital for plant growth and survival, is specified by the basic-helix-loop-helix (bHLH) heterodimers. Harnessing a new amination reaction, we here report a synthesis, target identification, and mode of action of an atypical doubly-sulfonylated imidazolone, Stomidazolone, which triggers stomatal stem cell arrest. Our forward chemical genetics followed by biophysical analyses elucidated that Stomidazolone directly binds to the C-terminal ACT-Like (ACTL) domain of MUTE, a master regulator of stomatal differentiation, and perturbs its heterodimerization with a partner bHLH, SCREAM. Guided by structural docking modeling, we rationally designed MUTE with reduced Stomidazolone binding. These engineered MUTE proteins are fully functional and confer Stomidazolone resistance *in vivo*. Our study identifies doubly-sulfonylated imidazolone as a direct inhibitor of the stomatal master regulator, further expanding the chemical space for perturbing bHLH-ACTL proteins to manipulate plant development.

46 **INTRODUCTION**

47

48 Plant growth and survival rely on stomata ~ adjustable vales on the shoot epidermis of land plants
49 facilitating efficient gas exchange while minimizing water loss. Each stoma consists of paired
50 guard cells that can adjust the aperture in response to the environment, such as light, drought,
51 and CO_2 levels [1]. A wealth of studies has elucidated the molecular basis of signaling mechanisms
52 leading to stomatal opening and closure [2,3]. In addition to stomatal movement, stomatal
53 development is also influenced by environmental conditions and in turn impacts plant's water-use
54 efficiency [4,5]. During leaf development, stomata are generated through a stereotypical sequence
55 of cell division and differentiation events [6,7]. In dicotyledonous plants, including Arabidopsis, the
56 stomatal-cell lineage is initiated via *de novo* asymmetric cell divisions in the protoderm, which
57 create meristemoids, proliferating stomatal precursor cells with a stem-cell-like property. After a
58 few rounds of asymmetric divisions, the meristemoid differentiates into a guard mother cell (GMC).
59 The GMC then undergoes a single symmetric division to terminally differentiate a stoma [8].
60 The cell-state transitional steps during stomatal development are governed by the
61 sequential actions of basic-helix-loop-helix (bHLH) transcription factors (TFs), SPEECHLESS
62 (SPCH), MUTE, and FAMA, which form heterodimers with their partner bHLHs, SCREAM (SCRM,
63 also known as ICE1) and SCRM2 [9-12]. The activities of these stomatal bHLH modules are enforced
64 by the inhibitory peptide-receptor kinase signaling pathways. Briefly, secreted peptide ligands
65 EPIDERMAL PATTERNING FACTORs (EPFs) are perceived by their receptors, ERECTA-family
66 receptor kinases and TOO MANY MOUTHS (TMM) [13-18]. This activates a downstream Mitogen
67 Activated Protein Kinase (MAPK) cascade, which in turn inhibits the bHLH heterodimers via direct
68 phosphorylation and degradation events [19-21].
69 Interestingly, these stomatal bHLH TFs possess a C-terminal ACT-Like (ACTL) domain, a
70 small structurally defined module resembling the ACT domain found in diverse metabolic
71 enzymes in bacteria and eukaryotes (named after aspartate kinase-chorismate mutase-tyrA
72 prephenate dehydrogenase) [21,22]. Recently, we revealed that the SCRM ACTL domain serves as
73 a heterodimer selectivity interface with SPCH, MUTE, and FAMA [23]. This rather surprising finding
74 offers a potential for the ACTL domain of bHLH TFs as a drug target for selective inhibition of
75 heterodimerization, hence stomatal differentiation. Whereas the ACTL domain is predominant
76 amongst plant bHLH proteins [24,25] no chemical inhibitors or binders targeting this domain, or more
77 broadly, bHLH-ACTL TFs are available.
78 Chemical compounds that selectively perturb functions and interactions of key regulatory
79 proteins can be a powerful tool to dissect and manipulate the development and physiology of cells

to whole organisms [26,27]. Stomata are not the exception [28]. For example, previous chemical screens identified compounds that suppress stomatal movement [29,30]. Likewise, small compounds have been utilized to examine the roles of signaling kinases and phosphatases in stomatal development [31-33]. Chemical library screens identified bubblin, which severely disrupts proper cell polarity in dividing meristemoids [34], as well as those that increase the number of stomata [35]. However, in all the above cases, the chemical compounds impact multiple processes, thus causing pleiotropic effects and/or their targets remain unidentified.

To expand a chemical space to control stomatal function and development, we have produced a collection of nitrogen-containing chemical compounds by utilizing a new amination reactions [36]. Nitrogen-containing molecules are widely recognized for their potent biological activities [37]. Previous chemical screens and subsequent structure-activity-relationship studies have shown that sulfonamidated compounds SIM1 (Stomata Influencing Molecule) and its derivative SIM3* inhibit stomatal movement [38]. Here, we report a complex doubly-sulfonylated imidazolone compound named Stomidazolone as a potent inhibitor of stomatal differentiation. We discover that Stomidazolone tightly binds to the MUTE ACTL domain and perturbs the MUTE-SCRM heterodimerization. We rationally designed Stomidazolone-resistant versions of MUTE and demonstrated their efficacy *in vivo*. Together with our chemical synthesis pipelines, our work will expand the chemical and pharmacological space for bioactive compounds and open the future directions for selective perturbation of prominent ACTL-domain containing plant bHLH TFs for transient manipulation of plant growth and development.

RESULTS

Doubly-sulfonylated imidazolone inhibits stomatal differentiation

In our initial attempt to derivatize SIM1 [38], we synthesized SIM1* from 2,4-diphenylimidazole through C–H imidation followed by monodesulfonylation, we serendipitously found the first one-shot synthesis of doubly-sulfonylated imidazolone (Fig. 1a; See Methods). Treatment of 2,4-diphenyloxazole with chloramine B in the presence of CuI afforded this doubly-sulfonylated, AYSJ929 (later named as Stomidazolone: Fig. 1a, Document S1 for synthesis and NMR spectra of the synthesized compounds). Further optimization produced Stomidazolone in 42% yield. Our new reaction enabled the conversion of diphenyloxazole into substituted imidazolone with two equivalents of chloramine (see Document S1). Even after searching the Reaxys database, we failed to uncover any records of a reaction that transforming diphenyloxazole into imidazolones.

114 The structure was unambiguously confirmed by X-ray crystallographic analysis, which clearly
115 shows the acute angular shape of this doubly-sulfonylated imidazolone (Fig. 1b, Table S1,
116 Supplementary Document S1). Unlike SIM1 and its derivative SIM3* [38], this compound did not
117 exhibit any discernable effects on stomatal movement using our standardized assays (Fig. S1).
118 The synthesized compound features numerous aryl groups, oxygen and nitrogen atoms
119 as hydrogen bond acceptors, as well as hydrogen atoms serving as hydrogen bond donors (see
120 Fig. 1b; Document S1), suggestive of potential bioactivity. We thus subjected it to our chemical
121 library screening pipeline for stomatal development [35]. Intriguingly, its application to Arabidopsis
122 seedlings conferred reduced number of stomata but concomitant increase in the number of
123 meristemoids (Fig. 1c). These increased meristemoids properly express both early and late
124 meristemoid reporter markers, *TMMpro::GUS-GFP* and *MUTEpro::nucYFP*, respectively (Fig. 1d).
125 Further quantitative analysis of stomata and meristemoid densities confirmed the dose-
126 dependency of the compound, now named Stomidazolone, to decrease the number of stomata
127 (24.45 %, 59.50 %, and 69.53 % decrease from mock to 20, 50, and 100 μM Stomidazolone,
128 respectively) while dramatically increasing the number of meristemoids (315.8 %, 801.5 %, and
129 647.6 % increase from mock to 20, 50, and 100 μM Stomidazolone, respectively) (Fig. 1e). On
130 the other hand, total number of stomata and meristemoids are only slightly reduced by the
131 Stomidazolone treatment (14.46 % and 25.03% at 20 and 50 μM) (Fig. 1e). These results suggest
132 that Stomidazolone inhibits stomatal differentiation at the transition from proliferating
133 meristemoids to differentiation. Stomidazolone does not affect overall seedling growth including
134 root elongation and cotyledon expansion, even at 100 μM (Fig. 1f). It is thus highly unlikely that
135 the observed inhibition of meristemoid differentiation is due to general seedling growth retardation.
136 We therefore conclude that Stomidazolone potently triggers the developmental arrest of the
137 meristemoids, and in a lesser extent, inhibits the stomatal-lineage initiation.
138

139 **Chemical genetics delineate Stomidazolone as a potential inhibitor of MUTE**

140 To unravel which pathways of stomatal development are impacted by Stomidazolone, we took a
141 chemical-genetic approach utilizing a series of mutants known to regulate stomatal development
142 (Fig. 2a). SPCH, MUTE, and FAMA consecutively drive stomatal-lineage progression [9-11] (Fig.
143 2a). To address whether Stomidazolone interferes with each cell-transitional step specified by
144 these stomatal bHLH proteins, we applied Stomidazolone to *spch*, *mute*, and *fama* mutant
145 seedlings. As shown in Fig. 2b and c, Stomidazolone exerted no effects on the pavement cell-
146 only epidermis of *spch*. Likewise, the arrested meristemoid phenotype of *mute* was not enhanced
147 by Stomidazolone. On the other hand, Stomidazolone significantly reduced the number of *fama*

148 tumors whereas increased the arrested meristemoids (Fig. 2c,d). Thus, *spch* and *mute* mutations
149 are epistatic to Stomidazolone, suggesting that this compound inhibits the MUTE-step of stomatal
150 fate commitment.

151 It is established that *ERECTA*-family genes interact synergistically to enforce stomatal
152 development [14]. Among them, *ERECTA* primarily inhibits the entry into stomatal cell lineages, a
153 process regulated by *SPCH*, whereas *ERECTA-LIKE1* (*ERL1*) restricts the differentiation
154 potential of the meristemoids, a process orchestrated by *MUTE* [39-41](Figs. 2a). The loss of function
155 in these receptor genes compromise the MAPK activation that inhibits SPCH and MUTE protein
156 accumulation [19,20,40]. Compared to wild type, *erecta* null allele (*er*: *er-105*) overly produces
157 stomatal-lineage cells [14] (Fig. 3a-d). Stomidazolone treatment exaggerated the *er-105* phenotype:
158 the number of stomata drastically reduced and the meristemoids vastly increased (Fig. 3a-d, k).
159 In *er erl1*, Stomidazolone treatment did not decrease the number of stomata, although it increased
160 the number of meristemoids (Fig. 3e, f, k). The result supports the previous finding that the loss
161 of *ERL1* intensifies stomatal differentiation by over-accumulation of MUTE [40], thereby conferring
162 partial resistance to Stomidazolone. The number of arrested meristemoids are even more
163 increased in *er erl2* (Fig. 3g, h), consistent with the loss of *ERL1* in this genetic background.
164 Finally, *er erl1 erl2* triple mutant seedlings appeared insensitive to Stomidazolone (Fig. 3i, j).
165 Combined, these rather complex results further support that Stomidazolone primarily interferes
166 with the MUTE activity for commitment to stomatal differentiation. Our results also suggest that if
167 ERECTA-family mediated signaling pathways are absent, Stomidazolone cannot effectively
168 interfere with the overly activated stomatal differentiation pathway.

169 It is known that HD-ZIP IV-family gene *HDG2* positively regulates stomatal differentiation
170 by promoting *MUTE* expression and that its paralog *AtML1* enhances the *hdg2* mutant phenotype
171 [42] (Fig. 2a). We next tested whether loss-of-function mutations in these genes enhance the effects
172 of Stomidazolone to trigger meristemoid arrests. As shown in Fig. 3l, m, Stomidazolone increased
173 the meristemoid numbers of *hdg2* epidermis while the total numbers of stomata and meristemoids
174 were unaffected. Strikingly, *hdg2 atml1* double mutant exhibited hypersensitivity to
175 Stomidazolone, and its application exaggerated *mute*-like epidermal phenotype (Fig. 3n, o).
176 Taken together, a series of chemical-genetic dissections indicates that Stomidazolone likely
177 inhibits the activity of MUTE.
178

179 ***In vivo* potency and selectivity of Stomidazolone relies on SCREAM**

180 SCRM is a heterodimeric partner of MUTE as well as SPCH and FAMA, and its activity is required
181 for stomatal cell-state transitions [12] (Fig. 2a). We investigated whether the activity of SCRM

182 influences the effects of Stomidazolone on stomatal differentiation. Strikingly, Stomidazolone
183 treatment to *scrm* loss-of-function mutant (also known as *ice1-2*) severely inhibited stomatal
184 lineage initiation, resulting in the *spch*-like epidermis vastly composed of pavement cells (Fig. 4a,
185 b). Conversely, Stomidazolone failed to inhibit the 'stomata-only' epidermis of *scrm-D*, a
186 constitutively active *SCRM* mutation that breaks the molecular bridge between MAPK cascade
187 and SPCH [12,21](Fig. 4c, d). Therefore, Stomidazolone's potency as an inhibitor of stomatal
188 differentiation relies on the activity of SCRM: In the absence of SCRM, Stomidazolone can
189 effectively inhibit the SPCH-regulated step of stomatal-lineage initiation. Under normal levels of
190 SCRM (i.e. in wild type), Stomidazolone predominantly triggers meristemoid arrest. Lastly, the
191 constitutively active form of SCRM is insensitive to Stomidazolone.
192 Next, we sought to delineate if Stomidazolone interferes with the *in vivo* heterodimerization
193 potential of SCRM. Recently, we have shown that the SCRM C-terminal ACTL domain serves as
194 a heterodimerization interface and its dysfunctions selectively abrogate heterodimerization of
195 SCRM with MUTE, but not SPCH [23]. We therefore used our sensitized mutants, *scrm-D_S343*
196 and *scrm-D_S423*, which encode scrm-D_{L484F} and scrm-$D_{\Delta ACTL}$, respectively [23]. Whereas both
197 *scrm-D_S343* and *scrm-D_S423* exhibit nearly wild-type epidermis, Stomidazolone triggered
198 excessive formation of arrested meristemoids [23] (Fig. 4 e-h). This phenotype resembles that of
199 *scrm-D mute* [43]. Taken together, our intricate *in vivo* phenotypic evidence highlights that
200 Stomidazolone inhibits meristemoid differentiation, most likely by disrupting the
201 heterodimerization of MUTE and SCRM through the C-terminal ACTL domain.
202
203 **Stomidazolone directly targets MUTE and interferes with its heterodimerization**
204 To address the molecular action of Stomidazolone, we investigated whether Stomidazolone
205 directly disrupts the heterodimerization of MUTE (as well as other stomatal-lineage bHLHs) with
206 SCRM. First, we performed yeast two-hybrid (Y2H) assays. The growth assays show that
207 Stomidazolone diminishes the association of SCRM with MUTE as well as with SPCH and FAMA
208 (note that the N-terminal activation domain of SPCH and FAMA have been removed to prevent
209 their autoactivation)[21] (Fig. 5a). Further quantitative α-galactosidase assays show that
210 Stomidazolone significantly inhibit these stomatal bHLH heterodimers, with slightly less impact on
211 the SPCH-SCRM heterodimers (Fig. 5b). A precursor analog of Stomidazolone, SIM3* acts as an
212 inhibitor of stomatal movement [38] (Fig. S2a). Unlike Stomidazolone, SIM3* has no effects on
213 stomatal development (Fig. S2b, c). Likewise, SIM3* does not affect heterodimerization of
214 stomatal bHLH proteins (Fig. S2d, e).

To quantitatively assess the direct inhibition of MUTE-SCRM heterodimers by Stomidazolone, we next performed two *in vitro* biophysical protein-protein interaction kinetics assays using biolayer interferometry (BLI) and isothermal titration calorimetry (ITC) (Fig. 5c, d; Fig. S3, Table S2). For this purpose, recombinant full-length SCRM and MUTE proteins were expressed and purified. Preincubation of Stomidazolone and MUTE decreased the binding affinity of MUTE and SCRM by two orders of magnitude for both BLI and ITC methods (Kd values increased from 7.5 ± 1.2 nM to 856.5 ± 15.1 nM in BLI and from 10.3 ± 2.1 nM and 1400 ± 40 nM in ITC for MUTE-SCRM binding with or without pre-incubation with Stomidazolone, respectively) (Figs. 5c, d, Fig. S3). These results demonstrate that Stomidazolone directly interferes with the MUTE-SCRM heterodimerization.

We next tested whether Stomidazolone directly binds to MUTE. Indeed, the BLI assay showed Stomidazolone binding to MUTE (Kd = 8.9 ± 1.2 μM) (Fig. 5e). In addition, we found that Stomidazolone binds with recombinant SPCH, FAMA, and SCRM proteins, albeit with lower affinity (Fig. 5e, Fig. S3, Table S3). Finally, to identify the binding domain of Stomidazolone on MUTE, we performed BLI assays with the purified recombinant bHLH domain and ACTL domain of MUTE. As shown in Fig. 5f, Stomidazolone specifically binds to the ACTL domain (Kd = 13.1 ± 1.3 μM). Again, Stomidazolone showed a lower affinity with the ACTL domains of SCRM, SPCH, and FAMA (Fig. S3, Table S3). Taken together, a series of yeast and *in vitro* studies demonstrates that Stomidazolone directly and preferentially targets the ACTL domain of MUTE and interferes with the MUTE-SCRM heterodimerization. Our results reinforce the previous finding that the ACTL domain integrity is strictly required for the heterodimerization of MUTE-SCRM, but not SPCH-SCRM or FAMA-SCRM [23], and further provide the molecular, mechanistic basis of Stomidazolone as an inhibitor of meristemoid differentiation.

Docking modeling identifies the Stomidazolone-MUTE binding interface

We demonstrated that the ACTL domain of MUTE is targeted by Stomidazolone (Fig. 5). To delineate the specific binding interface, we performed computational docking modeling (see Methods). Briefly, we used HADDOCK-based calculations to drive the docking process, using mutagenesis data and binding site information from Swiss Dock as ambiguous interaction restraints. Structural models showed that different racemic mixtures of Stomidazolone adopted the same geometry in all clusters, with ionic interactions mediated by charged residues within the MUTE ACTL domain, Arg-133 (R133), Arg-134 (R134), Glu-162 (E162), and Glu-163 (E163), and H-bonding and packing interactions by polar and hydrophobic residues Ile135, Val136, Thr164

248 and Val165 (Fig. 6a, b). The binding free energies of both racemic mixtures were similar (Table
249 S4).
250 Amino-acid sequence alignments of MUTE and its orthologs as well as their sister bHLHs
251 (SPCH and FAMA) show that R133 and R134 residues are highly conserved among the MUTE
252 and FAMA clades, whereas substitutions to His (H) and Lys (K) are prevalent in the SPCH clade
253 (Fig. S4). The E162 and E163 residues are replaced by Glu (E) and Gln (Q) and Asp (D) and D/E
254 in FAMA and SPCH clades, respectively (Fig. S4). Overall, the Stomidazolone-
255 SPCH/MUTE/FAMA ACTL domain binding interfaces possess positively and negatively charged
256 residues with clade-specific sequences, which might reflect the differences in physical binding
257 affinities (Fig. 5e, Fig. S2).
258 To confirm the predicted binding residues for Stomidazolone-MUTE interaction, we further
259 performed Alanine substitutions. For this purpose, we generated $MUTE_{R133A_R134A}$,
260 $MUTE_{E162A_E163A}$, and $MUTE_{R133A_R134A_E162A_E163A}$ mutants and then quantitatively analyzed
261 Stomidazolone binding affinity on these mutant versions of MUTE ACTL domain by using
262 biophysical assays, BLI and ITC (Fig. 6c, Fig. S2 and Table S3). In both assays, the binding
263 affinity was significantly reduced; The Kd values obtained for BLI assays are 85.6 ± 5.5 μM and
264 125.0 ± 12.0 μM for double mutants, and no binding was detected for the quadruple mutant (Fig.
265 6c). These results provide the experimental evidence for the predicted Stomidazolone-binding
266 interface of specific MUTE residues within its ACTL domain.
267
268 **Engineering Stomidazolone-resistance via a molecular docking modeling**
269 Our molecular docking modeling and experimental verification deciphered the Stomidazolone
270 binding interface at the MUTE ACTL domain (Fig. 6a, b). To the best of our knowledge, nothing
271 is known about the bioactivity of doubly-sulfonylated imidazolones nor drugs that target the ACTL
272 domains of bHLH TFs. We thus first explored the functional importance of the Stomidazolone-
273 binding sites within the MUTE ACTL domain. We expressed two different *MUTE* mutant versions
274 that are diminished in Stomidazolone binding (Fig. 6c) into *mute* knockout (*mute-2*) plants driven
275 by its own promoter (*MUTEpro::MUTE*$_{E162A_E163A}$*-GFP* and *MUTEpro:: MUTE*$_{R133A_R134A}$*-GFP*). We
276 in addition generated a control *MUTEpro::MUTE-GFP* construct using the identical molecular
277 cloning strategy, which was also transformed into *mute-2* in parallel (see Methods). Like the wild-
278 type MUTE-GFP, the engineered versions of MUTE-GFP are detected in the nucleus of a
279 differentiating meristemoid, and their expression fully rescued the *mute* arrested meristemoid
280 phenotype (Fig. 6d, e, Fig. S4a). These transgenic *mute* null lines grow into healthy, fertile plants
281 indistinguishable from the wild type. Thus, the site-directed mutations within the predicted

282 Stomidazolone-MUTE interaction interface do not impact the expression patterns or
283 functionalities of MUTE.
284 Next, we tested the effects of Stomidazolone. As expected, control *MUTEpro::MUTE-GFP*
285 *mute-2* seedlings significantly reduced the number of stomata upon Stomidazolone treatment (Fig.
286 6e, f, Fig. S5b, c). In contrast, independent lines of *MUTEpro::MUTE*$_{E162A_E163A}$*-GFP* and
287 *MUTEpro:: MUTE*$_{R133A_R134A}$*-GFP* exhibit Stomidazolone resistance, because Stomidazolone
288 treatment did not significantly affect the numbers of stomata and meristemoids (Fig. 6e, f, Fig.
289 S5b, c). These results validate the structurally modelled Stomidazolone-MUTE binding interface
290 and unambiguously demonstrate that the *in vivo* binding of Stomidazolone to the MUTE ACTL
291 domain is the cause of the inhibition of stomatal differentiation. Furthermore, our structure-guided
292 engineering of Stomidazolone-resistant plants suggests that the Stomidazolone-binding interface
293 within the ACTL domain can be uncoupled from the biological activity of the bHLH-ACTL TFs.
294
295
296 **DISCUSSION**
297 In this study, we developed a new catalytic amination and materialized a synthesis of
298 Stomidazolone, a complex, doubly-sulfonylated imidazolone that selectively inhibits stomatal
299 differentiation. Leveraged by the wealth of stomatal development mutant resources, our forward
300 chemical genetics pinpointed the exact *in vivo* target of Stomidazolone: the master regulator
301 MUTE. Further biochemical, biophysical, and structural modeling studies elucidated that
302 Stomidazolone perturbs the MUTE-SCRM heterodimerization through interacting with the ACTL-
303 domain of MUTE. Chemical synthesis of TF dimerization inhibitors is an under/unexplored field in
304 plant biology. As such, our work expands a chemical space for manipulation of developmental
305 processes.
306 Stomidazolone binds strongly to MUTE ACTL domain, but also exhibits weak *in vitro*
307 binding to other bHLH-ACTL proteins, including SPCH and FAMA, and interferes with their
308 heterodimerization *in vitro* and in yeast (Fig. 5e, Fig. S2). Nevertheless, selective inhibition of
309 meristemoid-to-GMC transition indicates that the MUTE-SCRM heterodimer is the primary *in vivo*
310 Stomidazolone target. It has been shown that heterodimerization of MUTE-SCRM, but not SPCH-
311 SCRM or FAMA-SCRM, relies on the presence or integrity of the SCRM ACTL domain [23]. Our
312 findings support the notion that the MUTE-SCRM pair is the most labile, hence druggable,
313 amongst the stomatal bHLH proteins. SPCH, MUTE, and FAMA are closely related paralogs. Yet,
314 they possess distinct domains, which may influence the efficacy of Stomidazolone. For instance,
315 SPCH has a MAPK-substrate domain, and its phosphorylation leads to SPCH protein

316 destabilization [19]. Interestingly, we found that mutants that decouple SPCH from MAPK-mediated
317 negative regulation are insensitive to Stomidazolone: they are complete loss of upstream receptor
318 kinases (*er erl1 erl2*)[14] and constitutively-active *scrm-D* that is unable to recruit MAPK to SPCH,
319 both causing exaggerated stomatal differentiation [12,21] (Figs 3i, j, 4b). It has been shown that, in
320 a rare instance, *er erl1 erl2* mutations can partially rescue the arrested meristemoid phenotype of
321 *mute* [44]. As such, the Stomidazolone-insensitivity phenotype of *er erl1 erl2* and *scrm-D* can be
322 explained by the overly-active and stable SPCH-SCRM heterodimers compensating for MUTE-
323 SCRM. This accords with the recent view hinting a hidden functional overlap between SPCH and
324 MUTE [45].

325 Our discovery that Stomidazolone targets functionally-dispensable residues within the
326 MUTE ACTL domain brings several implications. First, Stomidazolone (and its derivatives) could
327 be optimized in the future to map the functional significance of ACTL domains among the bHLH
328 TFs. The ACTL domain-containing bHLH proteins are prominent within the land plant lineages [24].
329 Whereas studies indicated the roles of the ACTL domains in dimerization [25], their functional
330 significance or mode of action remains largely unclear. In the well-studied case of Maize R, its
331 ACTL domain functions as auto-inhibitory homodimerization module that prevent the DNA binding
332 [46,47], a mechanism different from the stomatal bHLH-ACTL proteins [23]. Second, the finding hints
333 a hitherto unidentified small ligand-binding property of the ACTL-domain-containing bHLH
334 proteins. The prototypical ACT domain are found in biosynthetic enzymes and functions as a
335 sensor domain for small metabolic ligands, including amino acids and thiamine [22]. On the contrary,
336 it is unknown whether bHLH-ACTL TFs bind any endogenous small molecules. If they do, how
337 Stomidazolone interferes with such endogenous ligands would be interesting future direction.
338 Third, as we successfully achieved for MUTE (Fig. 6, Fig. S4), other bHLH-ACTL TFs could be
339 engineered to generate drug-resistant versions to selectively modulate plant phenotypes without
340 compromising their biological functions.

341 Harnessing synthetic chemistry to disrupt TF dimerization - while it seems like an obvious
342 means of manipulating growth and development, this approach is surprisingly unexplored in
343 plants. Studies identified small proteins that can competitively interfere with TF dimers and
344 prevent their DNA binding [48]. For instance, LONG HYPOCOTYL IN FAR-RED1 (HFR1) protein
345 titrates the bHLH TF, PHYTOCHROME INTERACTING FACTORs (PIFs), from forming functional
346 dimers [49]. In mammalian system, natural compound library screens have identified small
347 molecules that disrupt the homodimerization of the Hes1, an bHLH TF regulating neural cell
348 proliferation and differentiation [50,51]. In all these cases, unlike Stomidazolone, the inhibitors target

349 the core dimerization HLH modules that are essential for the TF function, thereby leaving little
350 room for designing and engineering the drug resistant versions of TFs.
351 In the synthetic chemistry point of view, the serendipitous discoveries of Stomidazolone
352 and subsequent chemical synthesis proffered a new catalytic transformation of oxazoles [37,52]. Our
353 newly discovered reaction can convert diphenyloxazole into imidazolone to create a highly
354 angular compounds (see Document S1), which are unexplored in a pharmacology field. Now that
355 we demonstrated this high degree of three-dimensionality of Stomidazolone interacts with a
356 discrete structural module of the ACTL domain and selectively inhibits the key step of stomatal
357 differentiation, further elaboration of our new amination reaction may expand the chemical space
358 for manipulating protein functions in plants and beyond.
359
360
361 **Materials and Methods**
362
363 **Materials availability**
364 Materials generated and used in this study will be available from Keiko Torii (ktorii@utexas.edu).
365 The synthesized imidazolones (Stomidazolone; ID-AYSJ929) may be limited in quantity. Inquiries
366 for availability could be directed to Kei Murakami (kei.murakami@kwansei.ac.jp).
367
368 **Plant growth condition and chemical treatment**
369 *Arabidopsis* accession Columbia (Col-0) was used as wild-type. The following mutants/transgenic
370 lines are reported elsewhere: *TMMpro::GUS-GFP* [13]; *spch-3/+, mute/+,* and *fama-1/+* [11]; *mute-*
371 *2/+* [44]; *MUTEpro::nucYFP* [40]; *ice1-2/scrm* (SALK_003155), *scrm2-1* (SAIL_808_B10) [12]; *er-105*
372 *erl1-2 erl2-1* [14]; *hdg2-2* (SALK_127828C) and *hdg2-2 atml1-3* (SALK_128172)[42], *scrm-D_S343*
373 and *scrm-D_S423* [23]. Their genotype and transcript reduction were confirmed. The presence of
374 transgenes/mutant alleles were confirmed by genotyping. Screening of small molecules that
375 reduce stomatal numbers was performed as previously described [35], in which all molecules were
376 dissolved in dimethyl sulfoxide (DMSO, Molecular biology grade, Fujifilm Wako, Japan 046-
377 21981), Col-0 seeds were sown in 96-well plates (TL5003; True Line) containing 95 μL of 1/2 MS
378 medium with rotary shaking at 140 rpm under continuous light at 22°C. Five μL of compounds
379 were dissolved in DMSO at 10 mM, and diluted with liquid 1/2 MS media to 1 mM and added on
380 1-day-old seedlings (final concentration, 50 μM). Seedlings were incubated for 8 days, and at day
381 9 seedling abaxial cotyledons were observed through confocal microscopy.
382

383 **Molecular cloning and generation of transgenic plants**

384 The following constructs for transgenic plants were generated in this study: *MUTEpro::MUTE-*
385 *GFP* (pAH11), *MUTEpro::MUTE*$_{E162AE163A}$*-GFP* (pHS133), *MUTEpro::MUTE*$_{R133AR134A}$*-GFP*
386 (pHS134). The original *MUTEpro::MUTE-GFP* construct (pLJP155) was generated via a different
387 cloning strategy with different antibiotics selection [11]. We therefore re-generate the wild-type
388 Three-way Gateway version of *MUTEpro::MUTE-GFP* (pAH11) as a control. *MUTE* genomic
389 coding construct without stop codon (pAR205) and *MUTE* promoter construct (pAR202) were
390 subjected to the Gateway reaction with R4pGWB504 [53]. The wild-type MUTE-GFP lines with the
391 identical R4pGWB504 backbone enable a proper comparison of phenotypic complementation.
392 The mutant versions of *MUTE* constructs were generated in the same way after the site-directed
393 mutagenesis using Q5 Site-directed mutagenesis kit (NEB) and subjected to the Three-Way
394 Gateway reaction after sequence confirmation. The constructs were then transformed into the
395 *Agrobacterium* strain GV3101 and floral dipped into *mute-2/+* plants. For detailed lists of oligo
396 DNA and plasmid information, see Tables S5 and S6, respectively.
397

398 **Confocal microscopy**

399 For confocal microscopy, cell peripheries of seedlings were visualized with propidium iodide
400 (Sigma, P4170). Images were acquired using LSM800 or LSM700 (Zeiss) using a 20x lens. The
401 GFP, YFP reporter and PI signals were detected with excitation at 488 nm and an emission filter
402 of 410 to 546 nm, at 488 nm and an emission filter of 410 to 546 nm, and with excitation at 561
403 nm and 582-617 nm emission range, respectively. Raw data were collected with 1024 x 1024
404 pixel images. For qualitative image presentation, Adobe Photoshop CS6 was used to trim and
405 uniformly adjust the contrast/brightness.
406

407 **Quantitative analysis of epidermal phenotype**

408 For quantitative analysis of the abaxial leaf epidermis, confocal images were taken on the days
409 after germination as indicated in the Figure legends. Preparation of images was done as
410 described previously [32,54]. For counting epidermal cell types, stomatal density, stomatal precursor
411 cells (meristemoids), total stomata-lineage cells (stomata and meristemoids) were calculated by
412 counting cell types in an area of 0.4 mm^2 (0.63 mm x 0.63 mm) and plotted as per mm^2. All raw
413 data are presented in Table S7.
414

415 **Yeast two hybrid assay**

Y2H assays were performed using the Matchmaker™ Two-Hybrid System (Clontech). Bait (pGBKT7) and prey (pGADT7) constructs were co-transformed into the yeast strain AH109 using Frozen-EZ Yeast Transformation II Kit (Zymo Research, T2001). The resulting transformants were spotted on SD (−Leu, −Trp) and SD (−Trp, −Leu, −His) selection media containing different concentrations of 3-amino-1,2,4-triazole (Sigma, A8056) as previously reported [21]. Quantitative α-galactosidase assay was also performed according to manufactural instruction (Clontech). Briefly, the transformants were incubated in 2 ml SD medium with 0, 10, 50 100 μM Stomidazolone or SIM3* with rotary shake (220 rpm) at 30°C overnight. The cultured media containing yeast were transferred to microtubes and centrifuged to obtain the supernatant. The colorimetric assay was performed by incubating 8 μL of supernatant with 24 μL Assay Buffer that contains 0.5 M sodium acetate (pH 4.5) (Nakalai tesque, 31137-25): 100 mM *p*-nitrophenyl α-D-Galactopyranoside Solution (Sigma N0877) = 2:1 (v/v) at 30°C for 60 min, then terminated by adding 960 μL 1X Stop Solution (0.1 M sodium carbonate, Fujifilm Wako 195-01582). After OD_{410} was recorded, α-galactosidase units were calculated according to the protocol (Clontech, P3024-1).

Chemical synthesis

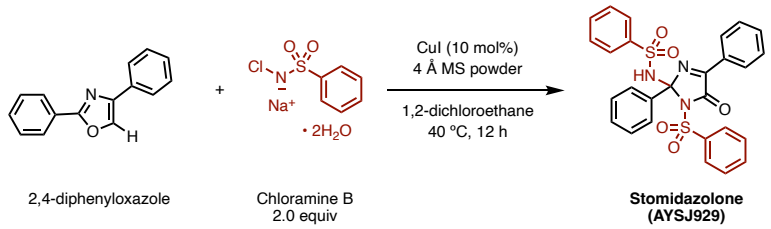

Synthesis of Stomidazolone (AYSJ929): 4 Å Molecular sieve powder (500 mg) was added into a large screw-capped tube and heat-dried in vacuo for 1 h. 2,4-Diphenyloxazole (111 mg, 0.50 mmol), Chloramine B dihydrate (250 mg, 1.0 mmol, 2.0 equiv) and CuI (9.5 mg, 50 μmol, 10 mol%) were added into the tube with a magnetic stirring bar in open air. The tube was evacuated and refilled with N_2 gas following the usual Schlenk technique. Anhydrous 1,2-dichloroethane (5.0 mL, 0.10 M) was added to the tube via the rubber top, the tube capped and its cap wrapped with parafilm. The reaction mixture was stirred and heated at 40 ºC for 12 h. The mixture was then cooled to room temperature, and the crude mixture was filtered through a pad of silica gel topped with Na_2SO_4 in a short column and concentrated *in vacuo*. Purification by flash chromatography on silica gel (hexane/ethyl acetate = 4:1) followed by recrystallization from CH_2Cl_2/methanol provided Stomidazolone (AYSJ929) in 42% yield (113 mg, 0.21 mmol) as a colorless crystal. For details of chemical synthesis see Document S1.

446

447 **NMR and mass-spectrometry**

448 The high-resolution mass spectra were recorded on Thermo Fisher Scientific Exactive Plus (ESI)
449 with Thermo Scientific Dionex UltiMate 3000 Series UHPLC or Agilent Technologies 6130
450 Quadrupole Liquid Chromatography/Mass Spectrometry (LC-MS). Nuclear magnetic resonance
451 (NMR) spectra were recorded on JEOL JNM-ECA-600 (^{1}H 600 MHz, ^{13}C 150 MHz) spectrometer.
452 Chemical shifts for ^{1}H NMR are expressed in parts per million (ppm) relative to residual $CHCl_3$ in
453 $CDCl_3$ (δ 7.26 ppm), and for ^{13}C NMR in ppm relative to $CDCl_3$ (δ 77.2 ppm). Data are reported
454 as follows: chemical shift, multiplicity (s = singlet, d = doublet, dd = doublet of doublets, t = triplets,
455 dt = doublet of triplets, td = triplet of doublets, tt = triplet of triplets, q = quartets, m = multiplets,
456 brs = broad singlet), coupling constant (Hz), and integration. For the original NMR and mass-
457 spectrometry data, see Dataset S1.

458

459 **X-ray crystallography**

460 A suitable crystal was mounted with mineral oil on a MiTeGen MicroMeshes and transferred to
461 the goniometer of the kappa goniometer of a RIGAKU XtaLAB Synergy-S system with 1.2 kW
462 MicroMax-007HF microfocus rotating anode (Graphite-monochromated Mo Kα radiation (λ =
463 0.71073 Å)) and HyPix6000HE hybrid photon-counting detector. Cell parameters were
464 determined and refined, and raw frame data were integrated using CrysAlis^{Pro} (Agilent
465 Technologies, 2010). The structures were solved by direct methods with SHELXT [55] and refined
466 by full-matrix least-squares techniques against F^2 (SHELXL-2018/3) by using Olex2 software
467 package [56]. The intensities were corrected for Lorentz and polarization effects. The non-hydrogen
468 atoms were refined anisotropically. Hydrogen atoms were placed using AFIX instructions. CCDC
469 2089650 contains the supplementary crystallographic data for this paper. These data can be
470 obtained free of charge from The Cambridge Crystallographic Data Centre via
471 www.ccdc.cam.ac.uk/data_request/cif. See Table S1 for X-ray crystallography data.

472

473 **Recombinant protein expression and purification**

474 *A. thaliana* SCRM1 (ICE1) (1-494), $_{\Delta N}$SPCH (98-364), MUTE (1-202), $_{\Delta N}$FAMA (190-414),
475 MUTE$_{\Delta C}$ (1-114), SCRM-ACT (405-494), MUTE-ACT (114-202), SPCH-ACT (285-364), FAMA-
476 ACT (306-414), MUTE$_{R133A_R134A}$, MUTE$_{E162A_E163A}$, MUTE$_{R133A_R134A_E162A_E163A}$ were cloned into
477 pGEX-4T-1 vector with an N-terminal GST tag and a thrombin cleavage sequence. For protein
478 expression, the constructs were transformed into *E. coli* strain BL21. For each transformant, a
479 single colony was selected and incubated in 10 ml LB liquid medium. The overnight-incubated *E.*

480 *coli* suspensions were transferred to 1L LB medium and incubated at 37 °C for around 2 h until
481 the OD_{600} reached 0.4–0.6. The isopropyl β-D-1-thiogalactopyranoside (0.25 μM of final
482 concentration) was added to the cultures and the strains were incubated at 22 °C for a further
483 18 h. GST-fused proteins were purified using glutathione agarose resin. The soluble portion of the
484 cell lysate was loaded onto a GST-Sepharose column. Nonspecifically bound proteins were
485 removed by washing the column with 20 mM Tris pH 8.0, 200 mM NaCl. The bound GST-fused
486 protein was eluted with 10 mm glutathione and 20 mM Tris pH 8.0, 200 mM NaCl. The GST-fused
487 proteins were exchanged with phosphate-buffered saline buffer, and then the solution was treated
488 with 50 μg of thrombin for 10–12 h at 16 °C. The GST portion of the protein was cleaved during
489 thrombin digestion, and then the whole solution was reloaded onto the glutathione *S*-transferase
490 column to obtain pure protein. The purified proteins were further purified by gel filtration on a
491 Superdex-200 (GE) column using fast protein liquid chromatography and phosphate buffer (pH
492 7.2) as the eluent. The purity of the protein was checked by SDS-PAGE. For detailed lists of oligo
493 DNA and plasmid information, see Tables S5 and S6, respectively.
494
495 **Isothermal titration calorimetry (ITC)**
496 Binding of the small molecule Stomidazolone to SCRM, MUTE, SPCH, FAMA, $MUTE_{\Delta C}$,
497 MUTE_ACTL, SCRM_ACTL, SPCH_ACTL and FAMA_ACTL, $MUTE_{R133A_134A}$, $MUTE_{E162A_163A}$,
498 $MUTE_{R133A_R134A_E162A_E163A}$, as well as SCRM binding to MUTE in the presence and absence of
499 Stomidazolone was characterized at 25 °C using a Malvern PEAQ-ITC microcalorimeter. All the
500 protein samples were dialyzed overnight using PBS buffer containing 2% DMSO. Stomidazolone
501 was dissolved in PBS buffer containing 2% DMSO. Titrations were performed by injecting 1 × 0.5-
502 μL and 12 × 3-μL aliquots of 1 mM Stomidazolone to 30 mM of protein in PBS buffer pH 7.4,
503 containing 2% DMSO. All titrations were carried out at least twice. The raw data were corrected
504 using buffer and protein controls and analyzed using the software supplied by the manufacturer.
505 See Table S3 for details.
506
507 **Biolayer interferometry (BLI)**
508 The binding affinities of the Stomidazolone with GST-tagged SCRM, MUTE, SPCH, FAMA, MUTE
509 ΔACTL, MUTE_ACTL, SCRM_ACTL, SPCH_ACTL and FAMA_ACTL, $MUTE_{R133A_134A}$,
510 $MUTE_{E162A_E163A}$, $MUTE_{R133A_R134A_E162A_E163A}$ were measured using the Octet Red96 system
511 (ForteBio, Pall Life Sciences) following the manufacturer's protocols. The optical probes coated
512 with anti-GST were first loaded with 500 nM GST tagged proteins before kinetic binding analyses.
513 The experiment was performed in 96-well plates maintained at 30 °C. Each well was loaded with

514 200 µL reaction volume for the experiment. The binding buffer used in these experiments
515 contained 1× PBS supplemented with 2% DMSO, 0.02% Tween20. The concentrations of the
516 Stomidazolone as the analyte in the binding buffer were 100, 50, 25, 12.5, 6.25, 3.12, and 1.56 µM.
517 There was no binding of the analytes to the unloaded probes as shown by the control wells.
518 Binding kinetics to all seven concentrations of the analytes were measured simultaneously using
519 default parameters on the instrument. The data were analyzed using the Octet data analysis
520 software. The association and dissociation curves were fit with the 1:1 homogeneous ligand
521 model. The k_{obs} (observed rate constant) values were used to calculate K_d, with steady-state
522 analysis of the direct binding. See Table S3 for details.
523

524 **Protein structural modelling**

525 MUTE and MUTE ACTL domain homology models were used from Alpha fold program
526 (https://alphafold.ebi.ac.uk/entry/Q9M8K6) The MUTE ACTL domain was subjected to
527 constrained energy minimization to allow the global energy minimization and structural analysis
528 using the AMBER 12 suite and VADAR [57,58]. Molecular docking of both racemic forms of
529 Stomidzolone to the MUTE, MUTE ACTL domain monomers was carried out using the high
530 ambiguity-driven biomolecular docking (HADDOCK) approach [59,60]. Ambiguous interaction
531 restraints (AIRs) were selected based on mutagenesis data and preliminary AUTODOCK model
532 [61]. The pairwise ligand interface RMSD matrix over all structures was calculated, and the final
533 structures were clustered using an RMSD cut-off value of 3.5 Å for both ligand and protein. The
534 clusters were then prioritized using RMSD and the HADDOCK score (weighted sum of a
535 combination of energy terms). See Table S4 for binding energies for Stomidazolone-MUTE
536 docking simulation.
537

538 **Measurement of stomatal opening in *Commelina benghalensis***

539 The experiments were performed as described previously [30,62]. Briefly, Stomidazolone or ABA
540 were added to a multi-well plate with basal buffer [5 mM MES/bistrispropane (pH 6.5), 50 mM KCl,
541 and 0.1 mM $CaCl_2$] to be diluted to a final concentration of 50 or 20 µM, respectively. *C.*
542 *benghalensis* plants were incubated in the dark overnight; then, 4 mm diameter leaf discs were
543 excised from fully expanded leaves using a hole punch (Biopsy Punch, Kai Medical). Samples
544 were immersed in a basal buffer containing compounds for 30 min before being exposed to light
545 (150 µmol m^{-2} s^{-1} red light and 50 µmol m^{-2} s^{-1} blue light) for 3 h. The stomatal apertures were
546 observed using a stereoscopic microscope (BX43; Olympus). The microscopic images were
547 acquired with a charge-coupled device (CCD) camera (DP27; Olympus), followed by autofocus

image processing using cellSens standard software (Olympus). Measurement of stomatal apertures of *C. benghalensis* was performed by using an automation program, *DeepStomata* [63].

Quantification and statistical analysis

A series of Z-stack confocal images was obtained to obtain images covering the epidermis and capturing GFP/YFP signal from the reporter lines. The area and the number of epidermal cells were quantified by using FIJI-ImageJ. Statistical analyses were performed using R ver. 4.0.2. Sample sizes (n) are indicated and defined in each legend. For the multiple sample comparison, 1-way ANOVA was performed followed by a post hoc Tukey HSD test. For the two-sample comparison, Student's T-test was performed. Graphs were generated using R ggplot2 package. For all boxplots, each box represents IQR (interquartile range), in which top, middle line, and bottom indicating 75, 50, and 25 percentiles, respectively, and the bar representing maximum to minimal values. Each dot represents jittered individual data point. The datapoints that go beyond the bar are outliers. The color of Boxplot graph was based on ColorBrewer.org. The value of n, the number of each experiment or samples, the means of error bars, and how statistical significance was defined are indicated in a relevant figure legend.

ACKNOWLEDGEMENTS

We thank Amanda Rychel and Alex Hofstetter for constructing the 3-Way Gateway version of *MUTEpro::MUTE-GFP*, Zixuan Li for assisting with chemical synthesis, Nagoya ITbM Molecular Structure Center for assistance in NMR and mass-spectrometry, Jason McLellan for the access to ITC, and Kosuke Watanabe for assistance with X-ray crystal structure analysis. We especially thank Yuichiro Tsuchiya for the insightful discussion and generously offering the lab space/facility for A.N., and Eundeok Kim for comments. A part of this work was conducted in Institute for Molecular Science supported by ARIM (JPMXP1223MS5012). This work was supported by MEXT/JSPS KAKENHI (16H01237, 17H06476 and 19H00990) to K.U.T.; Japan Science and Technology Agency (JST) PRESTO (JPMJPR20D8), TOBE MAKI Scholarship Foundation, and Tatematsu Foundation to K.M.; and ITbM Research Award to S.J.A.Y., A.N., and S.-K.H. A.N. was in part supported by the JST CREST Award (JPMJCR1924). S.J.A.Y. was supported by the JSPS Research Fellowship for Young Scientists DC1. S.-K.H. was supported by the Young Leader Cultivation Program from the Institute of Advanced Research, Nagoya University. K.U.T. acknowledges the support from the Howard Hughes Medical Institute and Johnson & Johnson Centennial Chair of Plant Cell Biology at UT Austin.

582
583
584 **CONTRIBUTIONS**
585 A.N., K.M., S.J.A.Y, S.-K.H and K.U.T. conceived the study. K.U.T., K.M., S.J.A.Y, S.K-H., A.N.,
586 and K.M.S. designed the experiments. A.N., K.M.S., S.J.A.Y, H.S., C.M.C., T.S., H.K., R.I, S.K.,
587 Y.A., K.U.T. performed the experiments (forward chemical genetics/transgenic/phenotypic
588 analysis A.N., S.J.A.Y, H.S., S.-K.H., C.M.C., H.K., K.U.T.; yeast/biochemical/biophysical
589 experiments, K.M.S., R.I.; chemical synthesis, K.M.; structural analyses/modeling, K.M., K.S.M.,
590 Y.S.; stomatal movement assays, Y.A., T.K.). A.N., K.S.M., K.M., Y.A. and K.U.T. performed data
591 analysis and visualization. K.U.T. wrote the manuscript draft. All authors contributed to the editing
592 of the manuscript. K.M. and K.U.T. are responsible for project administration and funding
593 acquisition.
594
595
596 **COMPETING INTERESTS**
597 The authors declare no competing interests.
598
599

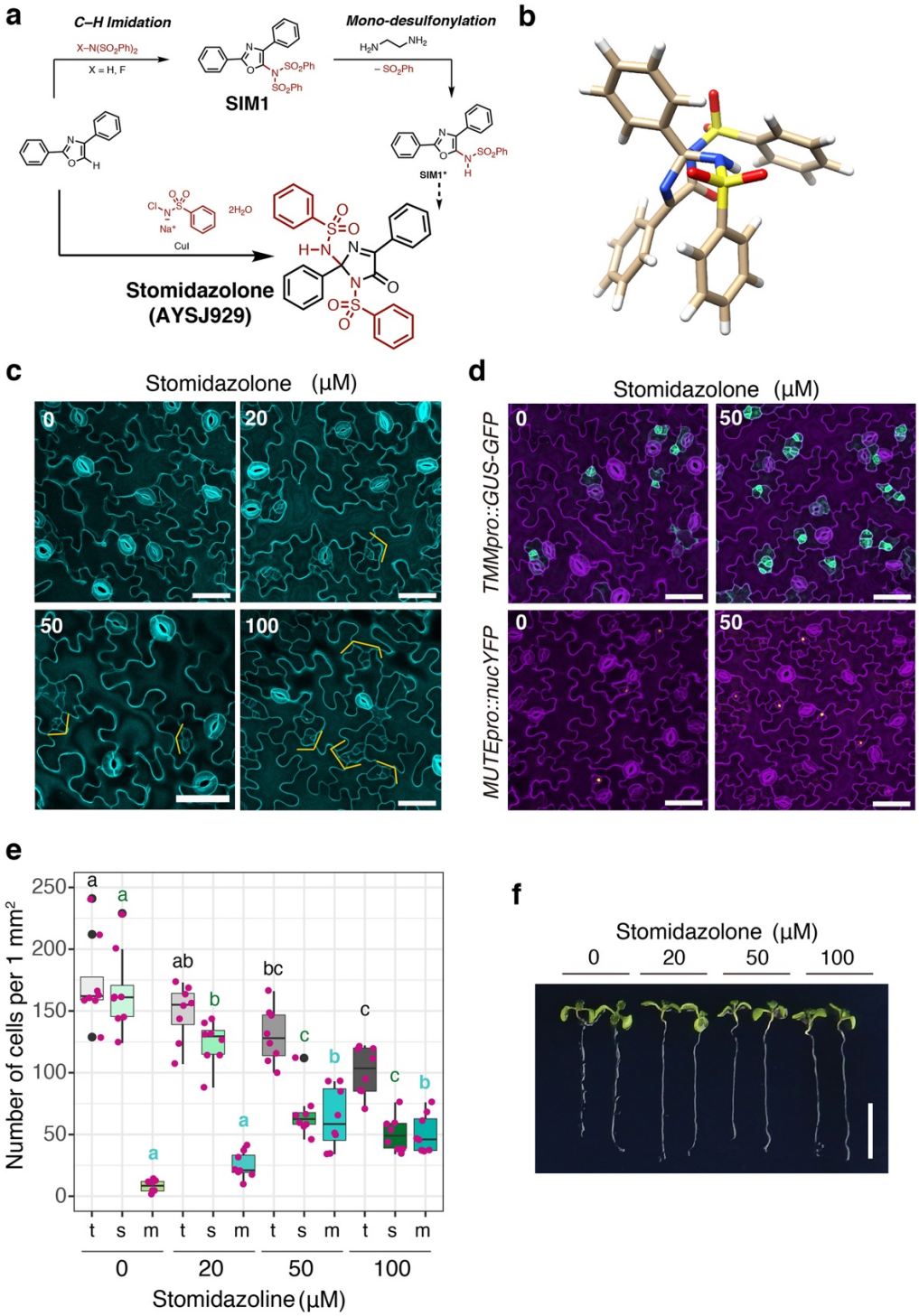

Figure 1. Stomidazolone is a potent chemical for meristemoid arrest

(a) Schematics of chemical synthesis. Supplementary Document S1 for the details of the synthesis. Bottom right, structure of Stomidazolone (ID: AYSJ929).

(b) X-ray crystal structure of Stomidazolone shown as a stick model (White, H; Beige, C; Blue, N; Yellow, S; Red, O).

607 (c) Confocal microscopy images of representative cotyledon abaxial epidermis from Arabidopsis
608 wild-type (WT) seedlings grown in the presence of 0 (mock), 20, 50, and 100 μM Stomidazolone.
609 Orange brackets, stomatal-lineage cells with an arrested meristemoid in the center. Scale bars,
610 50 μm.
611 (d) Arrested meristemoids by Stomidazolone express proper meristemoid markers. Shown are
612 confocal microscope images of representative abaxial cotyledons epidermis expressing
613 *TMMpro::GUS-GFP* (top) and *MUTEpro::nucYFP* (bottom) grown in the presence of 0 (mock:
614 Left) and 50 μM Stomidazolone (Right). Scale bars, 50 μm
615 (e) Stomidazolone treatment reduces the numbers of stomata but increases that of meristemoids.
616 Quantitative analysis of stomatal (s; green), meristemoid (m; cyan), and stomata+meristemoid (t;
617 gray) density per mm^2 of cotyledon abaxial epidermis from seedlings grown in the presence of 0
618 (mock), 20, 50, and 100 μM Stomidazolone. One-way ANOVA followed by Tukey's HSD analysis
619 were performed for each cell type (stomata and meristemoids). Letters (a,b,c) indicate groups
620 that are statistically different from other groups within each cell type. n = 8
621 (f) Stomidazolone does not impact seedling growth. Shown are two representative 9-day-old WT
622 seedlings, grown in the presence of 0 (mock), 20, 50, and 100 μM Stomidazolone. Scale bars, 10
623 mm.
624

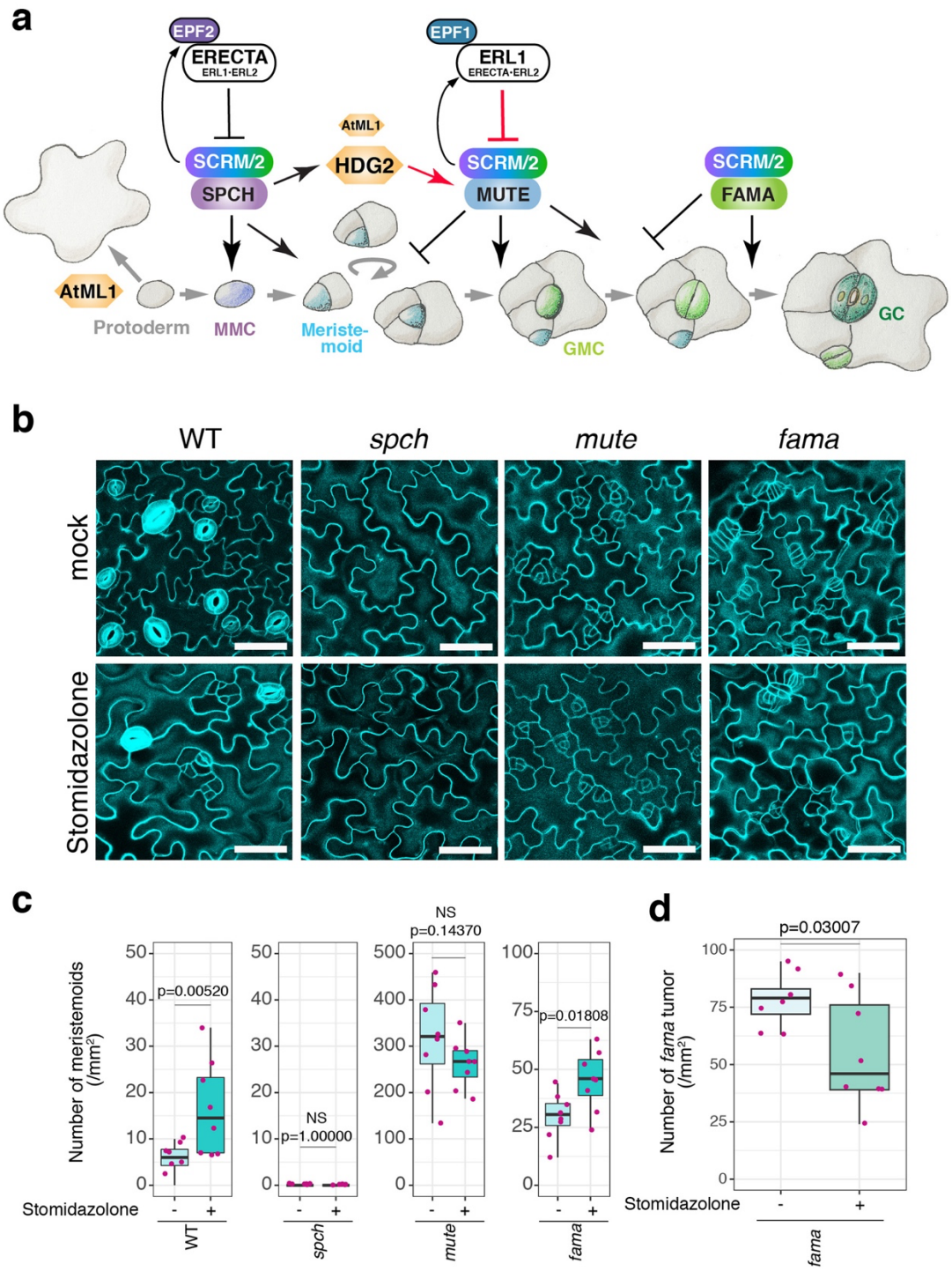

Figure 2. *spch* and *mute*, but not *fama*, are epistatic to Stomidazolone

(a) Schematic diagram showing the genetic control of stomatal cell-state transitions. Key genes/gene products and their roles are indicated in the cartoon. See main text for details of each step. Arrows, positive regulation; T-bars, negative regulation. Upregulation of *MUTE* by *HDG2* and inhibition of *MUTE* by *ERL1* are highlighted in red. MMC, meristemoid mother cell; GMC, guard mother cell; GC, guard cell.

633 (b) Representative cotyledon abaxial epidermis of mock and 50 μM Stomidazolone-treated WT,
634 *spch (spch-3)*, *mute (mute-1)*, and *fama*. Scale bars, 50 μm.
635 (c, d) Quantitative analysis of meristemoids density per 1 mm^2 (c) and *fama* tumors (d) of
636 cotyledon abaxial epidermis from seedlings grown in the presence of 0 (mock) and 50 μM
637 Stomidazolone. Student's T test was performed for each plant. p values and NS (not significant)
638 are indicated above each boxplot. n = 8.
639

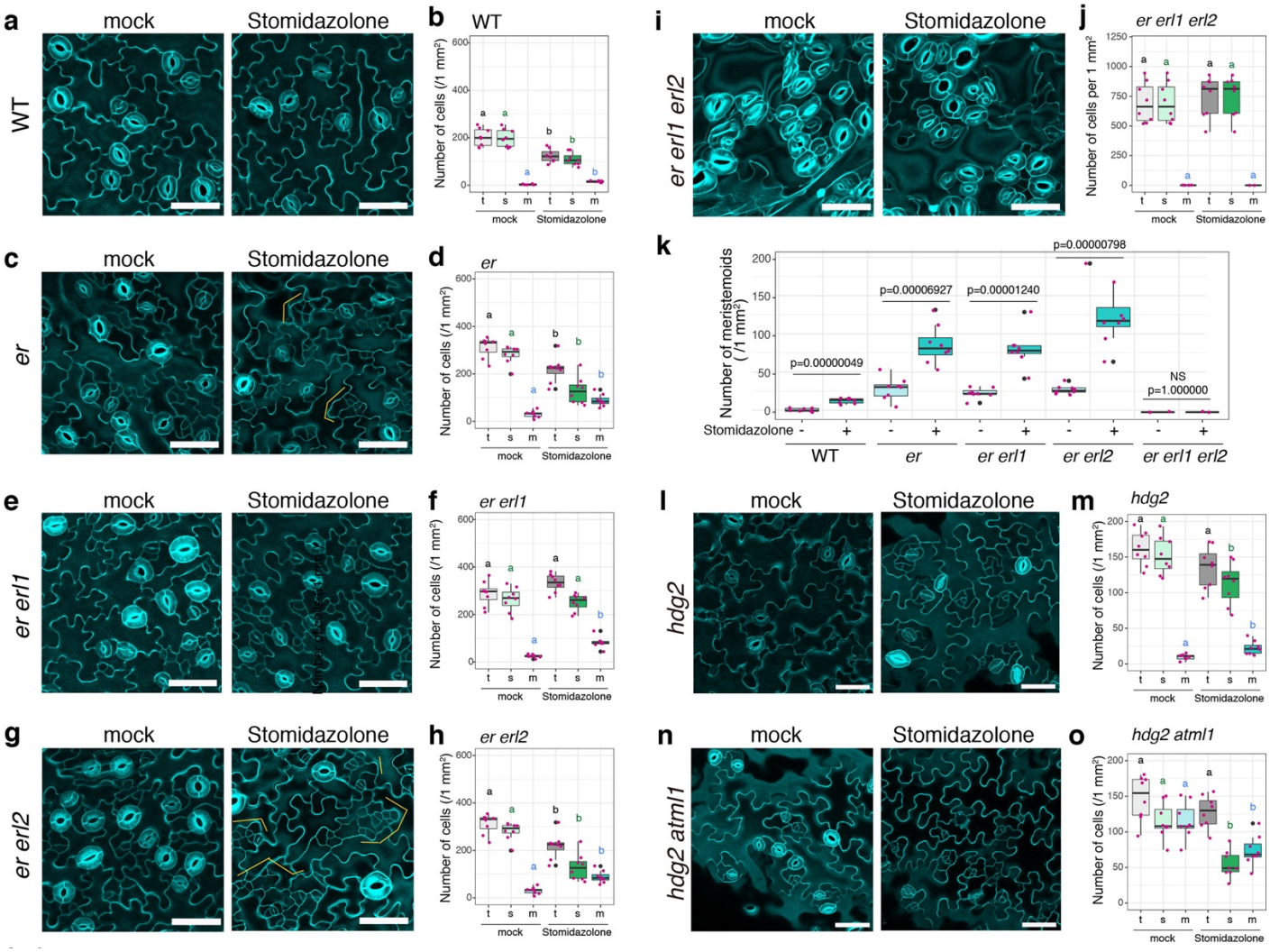

641

642 **Figure 3. Stomidazolone is a potent inhibitor of cell-state transition at the MUTE-step**

643 (a-j) Effects of Stomidazolone on the epidermis of wild-type (WT: a, b), *er* (c, d), *er erl1* (e, f), *er*
644 *erl2* (g, h), and *er erl1 erl2* (i, j). Representative cotyledon abaxial epidermis of mock- (left) and
645 50 μM Stomidazolone (right). Orange brackets, clusters of arrested meristemoids. Scale bars, 50
646 μm. (b, d, f, h, j) Quantitative analysis of stomatal (s; green), meristemoid (m; cyan), and
647 stomata+meristemoid (t; gray) density per mm^2 of cotyledon abaxial epidermis from seedlings
648 grown in the presence of 0 (mock) and 50 μM Stomidazolone. One-way ANOVA followed by
649 Tukey's HSD analysis were performed for each cell type (stomata and meristemoids). Letters
650 (a,b,c) indicate groups that are statistically different from other groups within each cell type. n =
651 8.

652 (k) Number of meristemods, data replotted from other panels.

653 (l-o) Effects of Stomidazolone on the epidermis of *hdg2* (*hdg2-2*: l, m) and *hdg2 atml1* (*hdg2-2*
654 *atml1-3*: n, o). All experiments and analyses were performed as described above. Scale bars, 50
655 μm. n = 8.

656

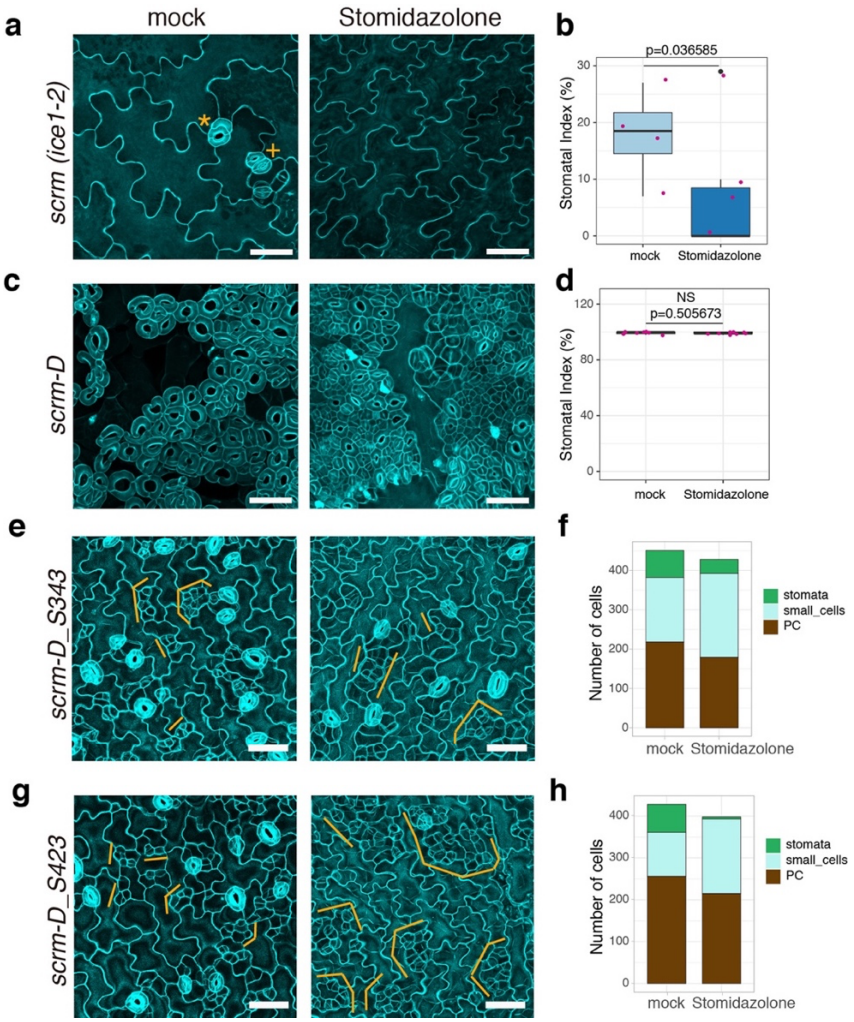

Figure 4. SCRM activity dictates *in vivo* potency and selectivity of Stomidazolone

(a) Abaxial epidermis of cotyledons in *scrm* (*ice1-2*) mutants treated with mock or 50 μM Stomidazolone on 1-day-old seedlings and further incubated for 8 days. *scrm* loss-of-function mutants occasionally exhibit parallelly paired-stomata, so called 'four-lips' phenotype (orange plus) as well as stoma made with extra guard cell (orange asterisk) likely due to FAMA mis-regulation. Scale bars, 50 μm.

(b) Stomatal index (SI, %) for Mock- or Stomidazolone-treated *scrm* mutant. n=8.

(c) Abaxial epidermis of cotyledons in *scrm-D* mutants treated with mock or 50 μM Stomidazolone on 1-day-old seedlings and further incubated for 8 days. Scale bars, 50 μm.

(d) Stomatal index (SI, %) for Mock- or Stomidazolone-treated *scrm-D* mutant. Student's T test was performed, and p values are shown above each boxplot. n=8.

(e-h) Effect of Stomidazolone on the epidermis of *scrm-D_S343* and *scrm_D_S423*. (e, g) Abaxial epidermis of cotyledons in *scrm-D_S343 and scrm_D_S423* mutants treated with mock or 50 μM Stomidazolone for 8 days. Clustered meristemoids and their sister stomatal-lineage ground cells (SLGCs: orange brackets) become exaggerated. Scale bars, 50 μm. (f, h) The cumulative bar graphs indicate the densities of stomata (green), small cells (meristemoids and SLGCs, cyan) and pavement cells (PC; dark brown) per 0.41 mm^2 with mock or 50 μM Stomidazolone.

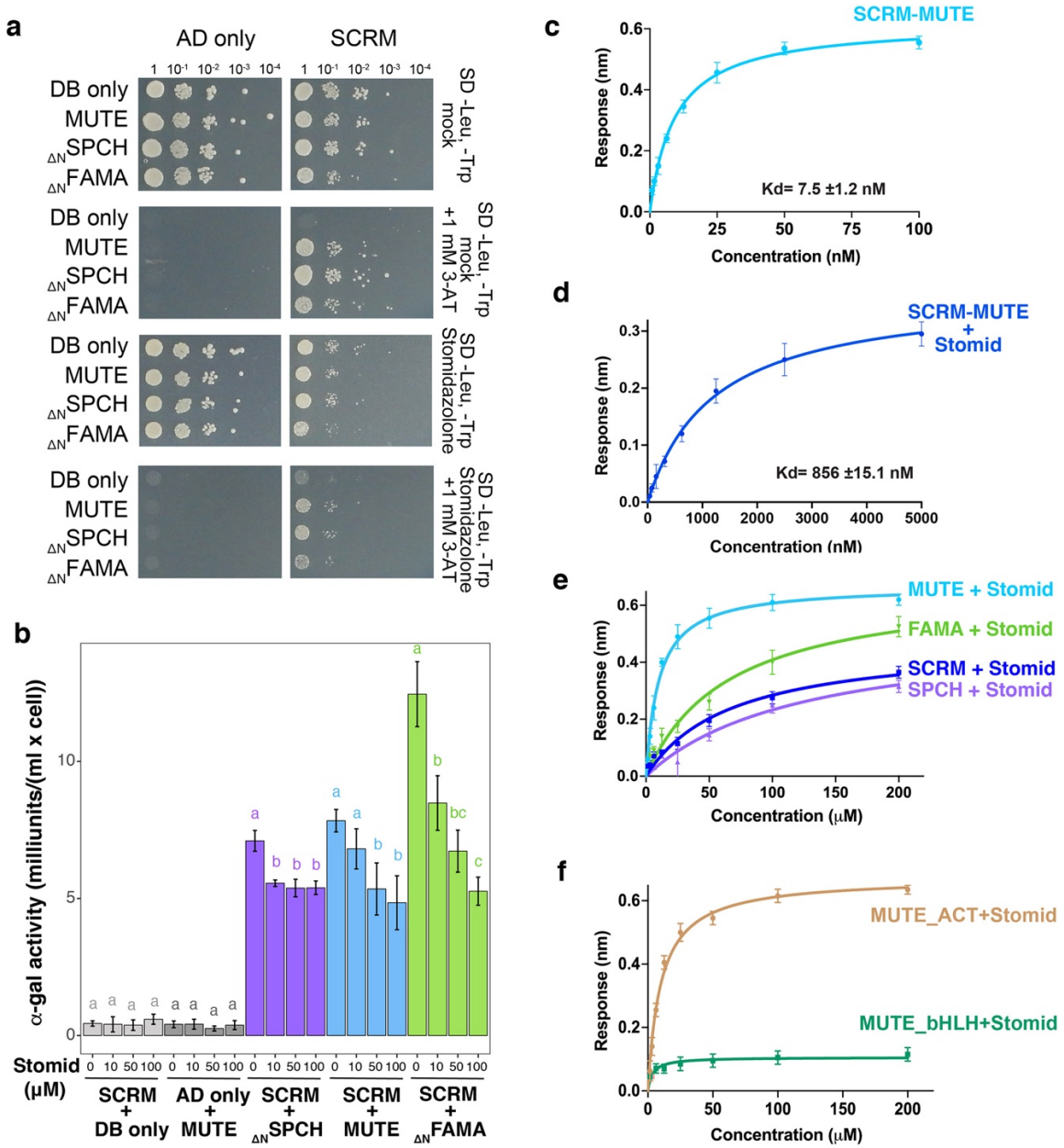

Figure 5. Stomidazolone binds to the ACTL domain and disrupts bHLH heterodimers

(a) Y2H analysis. Yeasts expressing control and pairs of stomatal bHLH proteins were spotted in 10-fold serial dilutions on appropriate selection media with or without 50 μM Stomidazolone. 1 mM 3-AT treatment shows that Stomidazolone reduces the interactions of SCRM with stomatal bHLH proteins. 3-AT, 3-amino-1,2,4-triazole.

(b) Quantitative α-galactosidase assays. Yeasts expressing control and pairs of stomatal bHLH proteins were cultured in 0, 10, 50, and 100 μM Stomidazolone and enzyme assays were performed. One-way ANOVA followed by Tukey's HSD analysis were performed. Letters (a,b,c) indicate that the enzyme activities are statistically different within the group. Experiments were repeated at least 3 times.

688 (c, d) Quantitative Analysis of SCRM-MUTE Interactions in the absence (c), and presence (d) of
689 Stomidazolone. *In vitro* binding response curves are provided for SCRM with MUTE and
690 with/without Stomidazolone. The data represent the mean ± SD and are representative of two
691 independent experiments.
692 (e) Quantitative analysis of Stomidazolone binding with SCRM (blue), MUTE (cyan), FAMA
693 (green), and SPCH (lavender). The MUTE protein exhibit higher affinity to Stomidazolone. *In vitro*
694 binding response curves are provided Stomidazolone with SCRM/MUTE/SPCH/FAMA/MUTE.
695 The data represent the mean ± SD and are representative of two independent experiments.
696 (f) Quantitative analysis of Stomidazolone binding with MUTE bHLH (green) and ACTL (brown)
697 domains. *In vitro* binding response curves are provided for Stomidazolone with $MUTE_{bHLH}$ and
698 $MUTE_{ACTL}$. The data represent the mean ± SD and are representative of two independent
699 experiments.
700
701

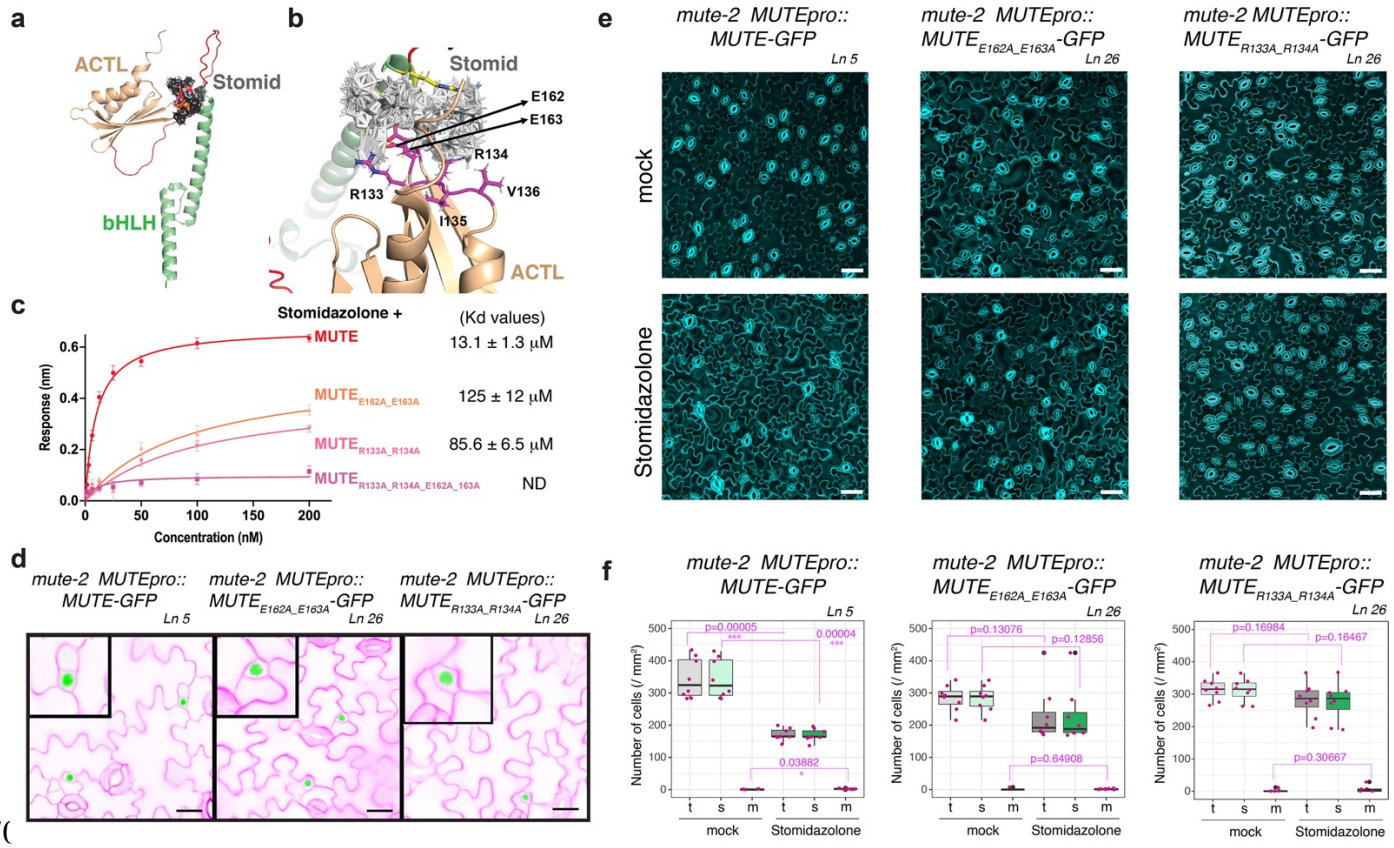

Figure 6. Engineering Stomidazolone-resistant plants based on the MUTE-Stomidazolone docking model

(a, b) MUTE-Stomidazolone binding models. (a) Alphafold2 predicted full-length MUTE protein is shown as ribbon representation. MUTE bHLH domain, green; ACTL domain, peach; Linker region, red. Stomidazolone is shown as stick model (gray). (b) Magnified view of MUTE-Stomidazolone binding interface. The key binding residues (R133, R134, E162 and E163) sidechains are highlighted in magenta.

(c) Quantitative analysis of Stomidazolone binding to wild-type MUTE and MUTE site-directed mutants ($MUTE_{R133A_R134A}$, $MUTE_{E162A_E163A}$, $MUTE_{R133A_R134AE162A_E163A}$) by BLI. *In vitro* binding response curves are presented for Stomidazolone with MUTE and its mutants. Stomidazolone compound was tested at seven different concentrations (200, 100, 50, 25, 12.5, 6.25, and 3.125 μM). The data represent the mean ± SD and are representative of two independent experiments.

(d) Site-directed mutant versions of MUTE that disrupt Stomidazolone binding are expressed normally and biologically functional. Representative cotyledon abaxial epidermis of 5-day-old *mute-2* seedlings expressing *MUTEpro::MUTE-GFP* (left), *MUTEpro::*$MUTE_{E162A_E163A}$ *-GFP* (center), and *MUTEpro::*$MUTE_{R133A_R134A}$*-GFP* (right). Insets, representative late meristemoids from each panel with MUTE-GFP signals in nucleus. Confocal images are inverted for clear cellular outlines. Scale bars, 20 μm.

(e-f) MUTE mutant versions that disrupt Stomidazolone binding confer drug resistance *in vivo*. (e) Representative cotyledon abaxial epidermis of five-day-old *mute-2* seedlings expressing *MUTEpro::MUTE-GFP* (left), *MUTEpro::*$MUTE_{E162A_E163A}$ *-GFP* (center), and

725 *MUTEpro::MUTE$_{R133A_R134A}$-GFP* (right) with mock- (top) and 20 μM Stomidazolone for eight days
726 (bottom). Scale bars, 50 μm.
727 (f) Quantitative analysis of total (t: stomata and meristemoids), stomatal (s: green) or meristemoid
728 (m: light cyan) density per mm^2 of cotyledon abaxial epidermis from seedlings grown in the
729 presence of 0 (mock) and 20 μM Stomidazolone. Student's T test was performed were performed
730 for each cell type (total, stomata and meristemoids) and p values are indicated. *, $p<0.05$, ***,
731 $p<0.0005$. Experiments were repeated twice. n = 8.
732
733
734
735

736 **REFERENCES**

737 1 Hetherington, A. M. & Woodward, F. I. The role of stomata in sensing and driving
738 environmental change. *Nature* **424**, 901-908 (2003).
739 2 Hsu, P. K., Dubeaux, G., Takahashi, Y. & Schroeder, J. I. Signaling mechanisms in
740 abscisic acid-mediated stomatal closure. *Plant J* **105**, 307-321 (2021).
741 3 Kim, T. H., Bohmer, M., Hu, H., Nishimura, N. & Schroeder, J. I. Guard cell signal
742 transduction network: advances in understanding abscisic acid, CO2, and Ca2+ signaling.
743 *Annu Rev Plant Biol* **61**, 561-591 (2010).
744 4 Qi, X. & Torii, K. U. Hormonal and environmental signals guiding stomatal development.
745 *BMC Biol* **16**, 21 (2018).
746 5 Bertolino, L. T., Caine, R. S. & Gray, J. E. Impact of Stomatal Density and Morphology on
747 Water-Use Efficiency in a Changing World. *Front Plant Sci* **10**, 225 (2019).
748 6 Han, S. K. & Torii, K. U. Lineage-specific stem cells, signals and asymmetries during
749 stomatal development. *Development* **143**, 1259-1270 (2016).
750 7 Lau, O. S. & Bergmann, D. C. Stomatal development: a plant's perspective on cell polarity,
751 cell fate transitions and intercellular communication. *Development* **139**, 3683-3692 (2012).
752 8 Nadeau, J. A. & Sack, F. D. Stomatal development in Arabidopsis. *Arabidopsis Book* **1**,
753 e0066 (2002).
754 9 MacAlister, C. A., Ohashi-Ito, K. & Bergmann, D. C. Transcription factor control of
755 asymmetric cell divisions that establish the stomatal lineage. *Nature* **445**, 537-540 (2007).
756 10 Ohashi-Ito, K. & Bergmann, D. C. Arabidopsis FAMA controls the final
757 proliferation/differentiation switch during stomatal development. *Plant Cell* **18**, 2493-2505
758 (2006).
759 11 Pillitteri, L. J., Sloan, D. B., Bogenschutz, N. L. & Torii, K. U. Termination of asymmetric
760 cell division and differentiation of stomata. *Nature* **445**, 501-505 (2007).
761 12 Kanaoka, M. M., Pillitteri, L. J., Fujii, H., Yoshida, Y., Bogenschutz, N. L., Takabayashi, J.,
762 Zhu, J. K. & Torii, K. U. SCREAM/ICE1 and SCREAM2 specify three cell-state transitional
763 steps leading to arabidopsis stomatal differentiation. *Plant Cell* **20**, 1775-1785 (2008).
764 13 Nadeau, J. A. & Sack, F. D. Control of stomatal distribution on the Arabidopsis leaf surface.
765 *Science* **296**, 1697-1700 (2002).
766 14 Shpak, E. D., McAbee, J. M., Pillitteri, L. J. & Torii, K. U. Stomatal patterning and
767 differentiation by synergistic interactions of receptor kinases. *Science* **309**, 290-293 (2005).
768 15 Hara, K., Kajita, R., Torii, K. U., Bergmann, D. C. & Kakimoto, T. The secretory peptide
769 gene EPF1 enforces the stomatal one-cell-spacing rule. *Genes Dev* **21**, 1720-1725 (2007).
770 16 Hara, K., Yokoo, T., Kajita, R., Onishi, T., Yahata, S., Peterson, K. M., Torii, K. U. &
771 Kakimoto, T. Epidermal cell density is autoregulated via a secretory peptide, EPIDERMAL
772 PATTERNING FACTOR 2 in Arabidopsis leaves. *Plant Cell Physiol* **50**, 1019-1031 (2009).
773 17 Hunt, L. & Gray, J. E. The signaling peptide EPF2 controls asymmetric cell divisions during
774 stomatal development. *Curr Biol* **19**, 864-869 (2009).
775 18 Lee, J. S., Kuroha, T., Hnilova, M., Khatayevich, D., Kanaoka, M. M., McAbee, J. M.,
776 Sarikaya, M., Tamerler, C. & Torii, K. U. Direct interaction of ligand-receptor pairs
777 specifying stomatal patterning. *Genes Dev* **26**, 126-136 (2012).
778 19 Lampard, G. R., Macalister, C. A. & Bergmann, D. C. Arabidopsis stomatal initiation is
779 controlled by MAPK-mediated regulation of the bHLH SPEECHLESS. *Science* **322**, 1113-
780 1116 (2008).
781 20 Lampard, G. R., Lukowitz, W., Ellis, B. E. & Bergmann, D. C. Novel and expanded roles
782 for MAPK signaling in Arabidopsis stomatal cell fate revealed by cell type-specific
783 manipulations. *Plant Cell* **21**, 3506-3517 (2009).
784 21 Putarjunan, A., Ruble, J., Srivastava, A., Zhao, C., Rychel, A. L., Hofstetter, A. K., Tang,
785 X., Zhu, J. K., Tama, F., Zheng, N. & Torii, K. U. Bipartite anchoring of SCREAM enforces

786 stomatal initiation by coupling MAP kinases to SPEECHLESS. *Nat Plants* **5**, 742-754
787 (2019).
788 22 Grant, G. A. The ACT domain: a small molecule binding domain and its role as a common
789 regulatory element. *J Biol Chem* **281**, 33825-33829 (2006).
790 23 Seo, H., Sepuru, K. M., Putarjunan, A., Aguirre, L., Burrows, B. A. & Torii, K. U. Intragenic
791 suppressors unravel the role of the SCREAM ACT-like domain for bHLH partner selectivity
792 in stomatal development. *Proc Natl Acad Sci U S A* **119** (2022).
793 24 Lee, Y. S., Shiu, S. H. & Grotewold, E. Evolution and diversification of the ACT-like domain
794 associated with plant basic helix-loop-helix transcription factors. *Proc Natl Acad Sci U S*
795 *A* **120**, e2219469120 (2023).
796 25 Lee, Y. S., Herrera-Tequia, A., Silwal, J., Geiger, J. H. & Grotewold, E. A hydrophobic
797 residue stabilizes dimers of regulatory ACT-like domains in plant basic helix-loop-helix
798 transcription factors. *J Biol Chem*, 100708 (2021).
799 26 Spring, D. R. Chemical genetics to chemical genomics: small molecules offer big insights.
800 *Chem Soc Rev* **34**, 472-482 (2005).
801 27 McCourt, P. & Desveaux, D. Plant chemical genetics. *New Phytol* **185**, 15-26 (2010).
802 28 Kinoshita, T., Toh, S. & Torii, K. U. Chemical control of stomatal function and development.
803 *Curr Opin Plant Biol* **60**, 102010 (2021).
804 29 Kim, T. H., Hauser, F., Ha, T., Xue, S., Bohmer, M., Nishimura, N., Munemasa, S.,
805 Hubbard, K., Peine, N., Lee, B. H., Lee, S., Robert, N., Parker, J. E. & Schroeder, J. I.
806 Chemical genetics reveals negative regulation of abscisic acid signaling by a plant
807 immune response pathway. *Curr Biol* **21**, 990-997 (2011).
808 30 Toh, S., Inoue, S., Toda, Y., Yuki, T., Suzuki, K., Hamamoto, S., Fukatsu, K., Aoki, S.,
809 Uchida, M., Asai, E., Uozumi, N., Sato, A. & Kinoshita, T. Identification and
810 Characterization of Compounds that Affect Stomatal Movements. *Plant Cell Physiol* **59**,
811 1568-1580 (2018).
812 31 De Rybel, B., Audenaert, D., Vert, G., Rozhon, W., Mayerhofer, J., Peelman, F., Coutuer,
813 S., Denayer, T., Jansen, L., Nguyen, L., Vanhoutte, I., Beemster, G. T., Vleminckx, K.,
814 Jonak, C., Chory, J., Inze, D., Russinova, E. & Beeckman, T. Chemical inhibition of a
815 subset of Arabidopsis thaliana GSK3-like kinases activates brassinosteroid signaling.
816 *Chem Biol* **16**, 594-604 (2009).
817 32 Houbaert, A., Zhang, C., Tiwari, M., Wang, K., de Marcos Serrano, A., Savatin, D. V., Urs,
818 M. J., Zhiponova, M. K., Gudesblat, G. E., Vanhoutte, I., Eeckhout, D., Boeren, S., Karimi,
819 M., Betti, C., Jacobs, T., Fenoll, C., Mena, M., de Vries, S., De Jaeger, G. & Russinova,
820 E. POLAR-guided signalling complex assembly and localization drive asymmetric cell
821 division. *Nature* **563**, 574-578 (2018).
822 33 Bian, C., Guo, X., Zhang, Y., Wang, L., Xu, T., DeLong, A. & Dong, J. Protein phosphatase
823 2A promotes stomatal development by stabilizing SPEECHLESS in Arabidopsis. *Proc Natl*
824 *Acad Sci U S A* **117**, 13127-13137 (2020).
825 34 Sakai, Y., Sugano, S. S., Kawase, T., Shirakawa, M., Imai, Y., Kawamoto, Y., Sugiyama,
826 H., Nakagawa, T., Hara-Nishimura, I. & Shimada, T. The chemical compound bubblin
827 induces stomatal mispatterning in Arabidopsis by disrupting the intrinsic polarity of
828 stomatal lineage cells. *Development* **144**, 499-506 (2017).
829 35 Ziadi, A., Uchida, N., Kato, H., Hisamatsu, R., Sato, A., Hagihara, S., Itami, K. & Torii, K.
830 U. Discovery of synthetic small molecules that enhance the number of stomata: C-H
831 functionalization chemistry for plant biology. *Chem Commun (Camb)* **53**, 9632-9635
832 (2017).
833 36 Ito, E., Fukushima, T., Kawakami, T., Murakami, K. & Itami, K. Catalytic Dehydrogenative
834 C-H Imidation of Arenes Enabled by Photo-generated Hole Donation to Sulfonimide.
835 *Chem* **2**, 383-392 (2017).

836 37 Hili, R. & Yudin, A. K. Making carbon-nitrogen bonds in biological and chemical synthesis.
837 *Nat Chem Biol* **2**, 284-287 (2006).
838 38 Toda, Y., Perry, G. J. P., Inoue, S., Ito, E., Kawakami, T., Narouz, M. R., Takahashi, K.,
839 Aihara, Y., Maeda, B., Kinoshita, T., Itami, K. & Murakami, K. Identification of stomatal-
840 regulating molecules from de novo arylamine collection through aromatic C-H amination.
841 *Sci Rep* **12**, 949 (2022).
842 39 Horst, R. J., Fujita, H., Lee, J. S., Rychel, A. L., Garrick, J. M., Kawaguchi, M., Peterson,
843 K. M. & Torii, K. U. Molecular Framework of a Regulatory Circuit Initiating Two-
844 Dimensional Spatial Patterning of Stomatal Lineage. *PLoS Genet* **11**, e1005374 (2015).
845 40 Qi, X., Han, S. K., Dang, J. H., Garrick, J. M., Ito, M., Hofstetter, A. K. & Torii, K. U.
846 Autocrine regulation of stomatal differentiation potential by EPF1 and ERECTA-LIKE1
847 ligand-receptor signaling. *Elife* **6**, e24102 (2017).
848 41 Qi, X., Yoshinari, A., Bai, P., Maes, M., Zeng, S. M. & Torii, K. U. The manifold actions of
849 signaling peptides on subcellular dynamics of a receptor specify stomatal cell fate. *Elife* **9**
850 (2020).
851 42 Peterson, K. M., Shyu, C., Burr, C. A., Horst, R. J., Kanaoka, M. M., Omae, M., Sato, Y.
852 & Torii, K. U. Arabidopsis homeodomain-leucine zipper IV proteins promote stomatal
853 development and ectopically induce stomata beyond the epidermis. *Development* **140**,
854 1924-1935 (2013).
855 43 Pillitteri, L. J., Peterson, K. M., Horst, R. J. & Torii, K. U. Molecular profiling of stomatal
856 meristemoids reveals new component of asymmetric cell division and commonalities
857 among stem cell populations in Arabidopsis. *Plant Cell* **23**, 3260-3275 (2011).
858 44 Pillitteri, L. J., Bogenschutz, N. L. & Torii, K. U. The bHLH protein, MUTE, controls
859 differentiation of stomata and the hydathode pore in Arabidopsis. *Plant Cell Physiol* **49**,
860 934-943 (2008).
861 45 Smit, M. E. & Bergmann, D. C. The stomatal fates: Understanding initiation and
862 enforcement of stomatal cell fate transitions. *Curr Opin Plant Biol*, 102449 (2023).
863 46 Kong, Q., Pattanaik, S., Feller, A., Werkman, J. R., Chai, C., Wang, Y., Grotewold, E. &
864 Yuan, L. Regulatory switch enforced by basic helix-loop-helix and ACT-domain mediated
865 dimerizations of the maize transcription factor R. *Proc Natl Acad Sci U S A* **109**, E2091-
866 2097 (2012).
867 47 Feller, A., Hernandez, J. M. & Grotewold, E. An ACT-like domain participates in the
868 dimerization of several plant basic-helix-loop-helix transcription factors. *J Biol Chem* **281**,
869 28964-28974 (2006).
870 48 Seo, P. J., Hong, S. Y., Kim, S. G. & Park, C. M. Competitive inhibition of transcription
871 factors by small interfering peptides. *Trends Plant Sci* **16**, 541-549 (2011).
872 49 Hornitschek, P., Lorrain, S., Zoete, V., Michielin, O. & Fankhauser, C. Inhibition of the
873 shade avoidance response by formation of non-DNA binding bHLH heterodimers. *EMBO*
874 *J* **28**, 3893-3902 (2009).
875 50 Arai, M. A., Masada, A., Ohtsuka, T., Kageyama, R. & Ishibashi, M. The first Hes1 dimer
876 inhibitors from natural products. *Bioorg Med Chem Lett* **19**, 5778-5781 (2009).
877 51 Arai, M. A., Makita, Y., Yamaguchi, Y., Kawano, H., Suganami, A., Tamura, Y. & Ishibashi,
878 M. Total synthesis of lindbladione, a Hes1 dimerization inhibitor and neural stem cell
879 activator isolated from Lindbladia tubulina. *Sci Rep* **10**, 21433 (2020).
880 52 Jiao, J., Murakami, K. & Itami, K. Catalytic methods for aromatic C–H amination: an ideal
881 strategy for nitrogen-based functional molecules. *ACS Catalysis* **6**, 610-633 (2016).
882 53 Nakagawa, T., Nakamura, S., Tanaka, K., Kawamukai, M., Suzuki, T., Nakamura, K.,
883 Kimura, T. & Ishiguro, S. Development of R4 gateway binary vectors (R4pGWB) enabling
884 high-throughput promoter swapping for plant research. *Biosci Biotechnol Biochem* **72**,
885 624-629 (2008).

54 Han, S. K., Herrmann, A., Yang, J., Iwasaki, R., Sakamoto, T., Desvoyes, B., Kimura, S., Gutierrez, C., Kim, E. D. & Torii, K. U. Deceleration of the cell cycle underpins a switch from proliferative to terminal divisions in plant stomatal lineage. *Dev Cell* **57**, 569-582 e566 (2022).

55 Sheldrick, G. M. SHELXT - integrated space-group and crystal-structure determination. *Acta Crystallogr A Found Adv* **71**, 3-8 (2015).

56 Dolomanov, O. V., Bourhis, L. J., Gildea, R. J., Howard, J. A. K. & Puschmann, H. OLEX2: a complete structure solution, refinement and analysis program. *J Appl Cryst* **42**, 339-341 (2009).

57 Case, D. A., Darden, T. A., Cheatham III, T. E., Simmerling, C. L., Wang, J., Duke, R. E., Luo, R., Merz, K. M., Wang, B., Pearlman, D. A., Crowley, M., Brozell, S., Tsui, V., Gohlke, H., Mongan, J., Hrnak, V., Cui, G., Beroza, P., Schafmeister, C., Caldwell, J. W., Ross, W. S. & Kollman, P. A. Amber 9. (2004).

58 Willard, L., Ranjan, A., Zhang, H., Monzavi, H., Boyko, R. F., Sykes, B. D. & Wishart, D. S. VADAR: a web server for quantitative evaluation of protein structure quality. *Nucleic Acids Res* **31**, 3316-3319 (2003).

59 Dominguez, C., Boelens, R. & Bonvin, A. M. HADDOCK: a protein-protein docking approach based on biochemical or biophysical information. *J Am Chem Soc* **125**, 1731-1737 (2003).

60 de Vries, S. J., van Dijk, A. D., Krzeminski, M., van Dijk, M., Thureau, A., Hsu, V., Wassenaar, T. & Bonvin, A. M. HADDOCK versus HADDOCK: new features and performance of HADDOCK2.0 on the CAPRI targets. *Proteins* **69**, 726-733 (2007).

61 Morris, G. M., Huey, R., Lindstrom, W., Sanner, M. F., Belew, R. K., Goodsell, D. S. & Olson, A. J. AutoDock4 and AutoDockTools4: Automated docking with selective receptor flexibility. *J Comput Chem* **30**, 2785-2791 (2009).

62 Aihara, Y., Maeda, B., Goto, K., Takahashi, K., Nomoto, M., Toh, S., Ye, W., Toda, Y., Uchida, M., Asai, E., Tada, Y., Itami, K., Sato, A., Murakami, K. & Kinoshita, T. Identification and improvement of isothiocyanate-based inhibitors on stomatal opening to act as drought tolerance-conferring agrochemicals. *Nat Commun* **14**, 2665 (2023).

63 Toda, Y., Toh, S., Bourdais, G., Robatzek, S., MacLean, D. & Kinoshita, T. DeepStomata: Facial Recognition Technology for Automated Stomatal Aperture Measurement. *bioRxiv* p 365098. (2018).